

Highlights

Toward AI-enhanced online-characterization and shaping of ultrashort X-ray free-electron laser pulses

Kristina Dingel, Thorsten Otto, Lutz Marder, Lars Funke, Arne Held, Sara Savio, Andreas Hans, Gregor Hartmann, David Meier, Jens Viefhaus, Bernhard Sick, Arno Ehresmann, Markus Ilchen, Wolfram Helml

- Convolutional neural networks can be used to study X-ray free-electron laser pulses on the fly.
- We demonstrate this on the reconstruction of free-electron laser pulses generated by self-amplification of spontaneous emission with the help of angular streaking.
- Besides providing relevant X-ray pulse characteristics as the pulse duration and intensity structure, we investigate the dependencies of the characteristics and how these can be used to improve predictions and the interpretation of concurrent measurements, in this case the Auger decay time.
- Our here proposed procedure enables immediate online analysis and therefore live diagnostics and control of ongoing experiments at free-electron lasers.

Toward AI-enhanced online-characterization and shaping of ultrashort X-ray free-electron laser pulses

Kristina Dingel^{a,f,1,*}, Thorsten Otto^{a,1}, Lutz Marder^{b,f}, Lars Funke^e, Arne Held^e, Sara Savio^e, Andreas Hans^{b,f}, Gregor Hartmann^{c,f}, David Meier^{a,c,f}, Jens Viefhaus^{c,f}, Bernhard Sick^{a,f}, Arno Ehresmann^{b,f}, Markus Ilchen^{b,d,g}, Wolfram Helml^e

^aIntelligent Embedded Systems, University of Kassel, Wilhelmshöher Allee 73, 34121 Kassel, Germany

^bInstitut für Physik und CINSaT, Universität Kassel, Heinrich-Plett-Straße 40, 34132 Kassel, Germany

^cHelmholtz-Zentrum Berlin für Materialien und Energie, Albert-Einstein-Straße 15, 12489 Berlin, Germany

^dEuropean XFEL GmbH, Holzkoppel 4, 22869 Schenefeld, Germany

^eTechnische Universität Dortmund, Fakultät für Physik, Maria-Göppert-Mayer-Straße, 44227 Dortmund, Germany

^fArtificial Intelligence Methods for Experiment Design (AIM-ED), Joint Lab Helmholtzzentrum für Materialien und Energie, Berlin (HZB) and University of Kassel

^gDeutsches Elektronen-Synchrotron DESY, Notkestraße 85, 22607 Hamburg, Germany

Abstract

X-ray free-electron lasers (XFELs) as the world's most brilliant light sources provide ultrashort X-ray pulses with durations typically on the order of femtoseconds. Recently, they have approached and entered the attosecond regime, which holds new promises for single-molecule imaging and studying nonlinear and ultrafast phenomena like localized electron dynamics. The technological evolution of XFELs toward well-controllable light sources for precise metrology of ultrafast processes was, however, hampered by the diagnostic capabilities for characterizing X-ray pulses at the attosecond frontier. In this regard, the spectroscopic technique of photoelectron angular streaking has successfully proven how to non-destructively retrieve the exact time-energy structure of XFEL pulses on a single-shot basis. By using artificial intelligence algorithms, in particular convolutional neural networks, we here show how this technique can be leveraged from its proof-of-principle stage toward routine diagnostics at XFELs, thus enhancing and refining their scientific access in all related disciplines.

Keywords: Angular streaking, Detector image analysis, Free-electron laser, Pulse characterization, Machine learning, Artificial intelligence, Simulation, Convolutional neural network

1. Introduction

Short-wavelength free-electron lasers (XFELs) are the world's fastest X-ray cameras, providing a spatial resolution down to the size of individual atoms. They yield ultrashort exposure times in the order of a millionth part of a billionth-second (*femtosecond*) which allows for 'freezing' the motion of atoms and molecules. In fact, XFELs have revolutionized several fields of science enabling us to observe the role of transient structures and resonances in single-molecule or cluster imaging [1], investigations of ultrafast processes at element-specific observer sites [2], and the study of nonlinear light-matter interaction in the X-ray regime [3].

Over the past decade, further development of the underlying machine operation techniques has enabled increasingly sophisticated control over the photon pulse parameters. One of the most recent major upgrades is the increased repetition rate of XFELs that is anticipated to initiate a leap from proof-of-principle experiments to advanced applications of interdisciplinary importance, thus representing a cornerstone of modern XFEL science [4].

XFELs worldwide are currently based on the principle of *self-amplification of spontaneous emission* (SASE) [5]. More precisely, their pulses are formed stochastically through the interplay between emitted synchrotron radiation caused by sinusoidally undulating electrons and their subsequent density modulation, resulting in ultrashort X-ray pulses of a peak brightness up to and exceeding $10^{32} \frac{\text{photons}}{\text{sec} \cdot \text{mrad}^2 \cdot \text{mm}^2 \cdot 0.1\% \text{BW}}$. This amplification process generates a non-predictable time-energy structure for every single pulse, constituting one of the biggest limitations for XFEL science so far. There are currently no control mechanisms and no routinely available diagnostics in place to *directly* measure the temporal properties of these X-ray pulses. Hence, the bulk of dynamics on attosecond to femtosecond time scales occurring during the exposure to the X-rays is unfortunately only inferred by indirect measurements such as spectral analysis [6] or electron beam diagnostics [7].

Recently, we have demonstrated a new technique termed *angular streaking* that is capable of retrieving the time-energy structure of all incoming SASE X-ray pulses non-destructively with attosecond resolution [8]. Besides the major diagnostic breakthrough, this generally paves the way for time-resolved and nonlinear attoscience in the X-ray regime. In fact, the onset of all structural dynamics in matter can now be studied in detail even from specific observer sites through strongly localized electrons. Fast and reliable feedback of this novel diagnostic re-

*Corresponding author.

E-mail address: kristina.dingel@uni-kassel.de

¹These authors contributed equally.

garding the experiment and the machine itself is of utmost importance for upcoming scientific applications at XFELs [9, 10]. For high-repetition-rate XFELs such as the European XFEL, conventional analysis approaches fail to accommodate the enormous amount and complexity of data in full depth. Especially for online analysis and, ultimately, (re)active control and pulse shaping during beam times, conventional data processing methods are not suited. Therefore, several core challenges of XFELs will be tackled by machine learning techniques.

In this article, we deliver a proof-of-concept on retrieving the full and detailed XFEL-pulse temporal profile, including the exact duration, its intensity substructure, and potential Auger decay processes initiated by the X-rays via the method of angular streaking paired with analysis through neural networks (NN). We use simulated streaking data with various degrees of instrument noise and different electron emission signatures to demonstrate the feasibility of implementing flexible and robust NN-based online diagnostic tools for XFELs.

After providing insights into the application case of angular streaking (Sec. 2), we elaborate on the design of the machine learning experiments (Sec. 3). We investigate the accuracy of their predictions in Sec. 4 and use it to make assumptions regarding enhanced future experiments at XFELs (Sec. 5).

2. Application Case: Angular Streaking

A long-standing goal in laser and X-ray research is to enable measurements providing both temporal and spatial real-time information about structural changes on a molecular level with element-site specificity (*molecular movie*). For this, a suitable ultrashort X-ray pulse duration is one of the key parameters, which is both hard to facilitate and difficult to measure. Yet, a reliable temporal measurement is essential for determining other parameters such as the detailed pulse-intensity profile [11], corresponding damaging thresholds for materials under investigation [12], the nanoscale interpretation of ultrafast single-shot diffraction imaging [13], and the probabilities for multi-photon processes [14, 15], to name a few.

Applying the *attoclock technique* to the field of XFELs leverages a versatile approach for the temporal and spectral characterization of individual (X)FEL pulses [8, 16]. The experimental results provide direct information about the full time-energy distribution of the stochastic X-ray pulses with attosecond resolution on a single-shot basis, including X-ray pulse duration, intensity substructure, and chirp.

The applied scientific instruments for this new method are *angle-resolving electron spectrometers* [8, 9]. In case of the first demonstration of angular streaking at XFELs and also in the present case, an array of 16 individually working time-of-flight (TOF) spectrometers is arranged in a ring-like structure around the target region, perpendicular to the propagation direction of the incoming X-rays [8]. Together with a co-propagating circularly polarized optical laser, spatially and temporally overlapped with the XFEL at the target region, this setup enables angular streaking. For this method, atoms from a target gas are ionized with the XFEL pulse and the emitted electrons are

swept in energy and angle by the concomitant rotating optical laser field. The target gas can be routinely adapted to the photon energy under diagnostic investigation in terms of providing appropriate electron binding energies and photoionization cross-sections. Thus, the temporal intensity distribution of the XFEL pulse is mapped to the streaked electron spectra, and their angle-dependent detection allows the necessary temporal characterization of XFEL pulses with attosecond resolution. The exact mechanism and experimental setup for the angular streaking technique as applied to SASE X-ray pulses is described in [8] and the general principle of two-color circular streaking can be found in [17, 18, 19].

In the current experiment under consideration, a time trace is measured for every X-ray shot and each TOF spectrometer, hence, generating 16 traces at a rate set by the repetition frequency of the XFEL in combination with the overlapped streaking laser. For single-shot spectroscopy, a trace represents the number of electrons arriving after specific flight times. These time-domain traces can be converted to the energy domain by taking into account the length of the flight path and potential additional electric fields along their path, which are routinely used for dispersing the electron further in time and thus enhancing the achievable energy resolution. In their accumulated representation over all angles (*detector image*), they are then put side-by-side, forming an image with 16 columns, representing the respective detector angles, and several rows corresponding to the range of electron energies detected in the specific measurement (cf. Fig. 2b). The energy-converted traces are called electron spectra, and the detector image is analogous to a *spectrogram*, where usually the x -axis displays the delay (time) steps instead of the angle coordinate (cf. Fig. 2a).

One can understand this relation through the correspondence of the electric field vector direction for the circularly polarized streaking laser with a certain phase value, allowing to identify each detector angle with an according time interval as a fraction of one full rotation cycle for the streaking field.

For an X-ray shot with no temporal and spatial overlap in the interaction region with an external streaking field (*unstreaked shot*), the spectra in all detectors are showing the characteristic distribution of lines for the atom under investigation. The *angular distribution anisotropy parameter* β_2 describes the undisturbed angular distribution. $\beta_2 = 0$ corresponds to completely isotropic emission, giving rise to the identical signal in each TOF (cf. Fig. 6d). $\beta_2 = 2$ specifies a \cos^2 -like emission pattern in the form of a dumbbell oriented in the direction of the (linear) X-ray polarization (cf. Fig. 6b).

If a *circularly polarized streaking laser* is present, the detector image gets modulated according to the streaking laser vector potential, leading to a sinusoidal variation of the spectral lines along the angle axis. This shape is influenced by the characteristics of the optical laser, some of which can change from shot to shot and are described later on. But there are also parameters of the streaking laser polarization that remain constant during the experiment:

The *ellipticity of the polarization* is defined as the ratio of the major axes of the polarization ellipse b/a . For perfectly circular polarization, this ratio amounts to unity, while it is equal

to zero for linear polarization. A small deviation from circular polarization gives rise to a certain degree of ellipticity, which manifests itself in a different maximum streaking amplitude of the electrons for the individual detectors. For an elliptically polarized optical beam, the principal axis may also have an arbitrary rotation (*elliptical tilt*) with respect to the ring of detectors, which is again unchanged throughout the experiment, but needs to be reconstructed for an unambiguous X-ray pulse retrieval.

The ultimate goal regarding X-ray pulse characterization and potential control is to reconstruct the spectrogram from a measured detector image, which gives the full information about the X-ray time–energy structure. However, in many experimental situations, it is sufficient to restrict our analysis to some of the most relevant SASE X-ray parameters. To get an impression on how well the machine learning algorithms work concerning experimentally easy as well as more difficult-to-measure parameters, we picked the following pulse characteristics and compared their relative reconstruction (*prediction*) accuracy with the originally simulated data (*target*):

Kick. The kick is the maximum streaking shift in terms of electron kinetic energy for each X-ray shot and thus for a given temporal delay and phase relation between the X-ray pulse and the optical streaking laser. There are two main reasons for a change in the kick from shot to shot. The first is the *relative timing jitter* between the X-ray and the streaking pulse [20, 21, 22], which is unavoidable due to the stochastic generation process of the SASE mechanism and additional fluctuations in arrival time caused by air fluctuations, thermal expansion in optomechanical components, and general synchronization errors between the two separate laser pulses. The second reason for variations of the kick is the *random change of the carrier-envelope phase* for the streaking laser from shot to shot. One can solve this by stabilizing the carrier-envelope phase [23], which is a rather difficult technical requirement, or by using the technique of angular streaking [8], which is the basis for the simulations studied in this article.

Pulse duration. The pulse duration is the most important parameter for many ultrafast free-electron laser experiments, e.g., a variety of pump/probe measurements of electronic state changes or investigations of nonlinear excitation dynamics [15, 24, 25, 26], albeit it is one of the most difficult to measure directly. Especially for XFEL SASE pulses, each pulse has a different duration and erratic intensity structure that even complicates the definition of the term *pulse duration*. In this article, we use the *root-mean-square deviation*, i.e., the square root of the second moment of the temporal intensity profile, as the definition of the *pulse duration*. We refrain from using the *full width at half-maximum*, which is a common choice for more well-behaved Gaussian-like laser pulses from table-top systems. As SASE pulses are generally spiky and irregularly (cf. Fig. 1), this metric is not fully applicable.

Pulse structure. Each SASE pulse has an individual profile, made up of several shorter ‘spikes’ with random intensity (cf. Fig. 1). The average number of spikes per pulse is determined by general parameters of the specific mode of XFEL

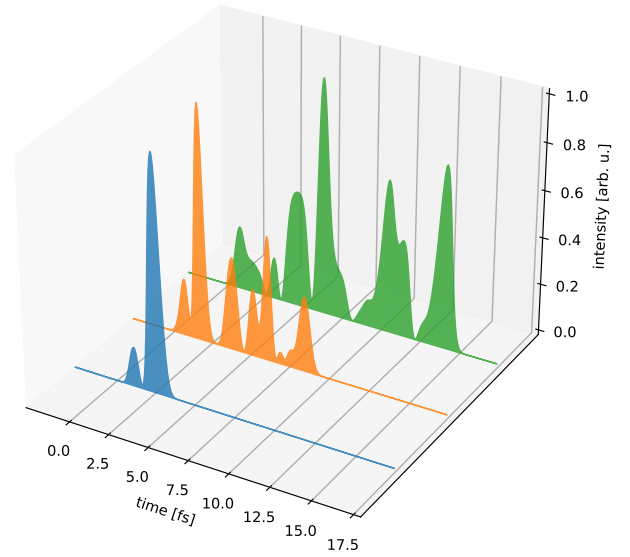


Figure 1: Three examples of different SASE XFEL pulse intensity structures showing varying total duration and complexity.

operation. It can be expressed in a statistical treatment as the number of individual energy modes contributing to the XFEL pulse [27]. The ensuing pulse shape can be arbitrarily complex. The shorter the overall pulse duration in relation to the single-spike length, i.e., the fewer spikes per complete pulse, the more important individual spikes are becoming (Fig. 1). Especially for estimating the damage thresholds of investigated probes as well as for experiments sensitive to the instantaneous X-ray intensity, or for ultrafast pump/probe measurements, the XFEL pulse structure needs to be known exactly to interpret the observed data on a shot-to-shot basis unambiguously. That is why the pulse structure is a fundamental and crucial parameter for all high-intensity dynamical or nonlinear X-ray experiments, while it is probably the most difficult property of SASE X-ray pulses to measure.

Decay time. Many of the scientifically interesting processes of non-equilibrium physics and structure-changing chemistry are not directly triggered by the exciting X-ray pulse but are the result of subsequent complex relaxation dynamics. These dynamics are determined by the time-dependent electronic structure of the system under study. A fundamental process taking place in atomic systems after inner-shell ionization by X-rays is the *Auger decay*, whereby a second electron from an outer shell fills the generated core hole and transfers the excess energy to a third electron (*Auger electron*), which is then emitted from the ion. This process is specific to the contributing discrete electronic states for a certain atomic or molecular system. It has a characteristic time constant for the emission of the third electron (*Auger decay time*). In our simulations, we assume an Auger decay channel dominating in Ne after 1s ionization, which has an Auger decay time on the order of 2 fs to 3 fs [28], serving as a fundamental benchmark for demonstrating the ultrafast time resolution capability of the method.

3. Machine Learning Procedure Design

In real-world XFEL experiments, the spectrograms of the respective SASE pulses are unknown. To reconstruct them, we must use the detector image only to draw conclusions about the underlying pulse characteristics (cf. Sec. 2). Despite available approaches to deriving pulse characteristics [29], they are only sparsely suitable for fast online processing during experimental campaigns. NNs, especially convolutional NNs, have already proven successful in image processing problems such as object detection [30, 31]. We will demonstrate their potential for our application case by guiding through the problem definition and the NN design in more detail.

3.1. Requirements

In order to train NNs in a supervised manner, we require training data \mathcal{D}_K of size $K \in \mathbb{N}$, which comprises of K simulated detector images $\mathcal{X} = \{\mathbf{X}_i \in \mathbb{M}^{m \times n}(\mathbb{R}), i = 1, \dots, K\}$ with K according pulse characteristics $\mathcal{L} = \{L_i \in \mathbb{R}_+^j, i = 1, \dots, K\}$. m is the number of TOFs used within the complete spectrometer setup. n displays the electron kinetic energy in arbitrary steps. The size of j changes according to the pulse characteristic that has to be predicted. In the following, we will refer to them as *labels*. To verify the performance of the NN, we split \mathcal{D}_K into two distinct sets, $\mathcal{D}_{\text{train}}$ and $\mathcal{D}_{\text{test}}$, such that $\mathcal{D}_K = \mathcal{D}_{\text{train}} \cup \mathcal{D}_{\text{test}}$. The accuracy of the NN is determined by $\mathcal{D}_{\text{test}}$. To avoid overfitting of the NN, we utilize *cross-validation*.

Although we work in a simulation environment only, it is reasonable to choose values that would correspond to real experimental data. Therefore, we use previously acquired data from earlier campaigns as introduced in Sec. 2. Concretely this means:

- We generate a size of $K = 4.4 \cdot 10^6$ samples for each label. Of these, $4 \cdot 10^6$ are used for training and $4 \cdot 10^5$ for testing.
- Our angle-resolved spectrometer consists of $m = 16$ TOF detectors.
- We fix the number of steps along the energy axis to $n = 200$, with an accordingly varying energy bin size spanning the respective spectral range of interest.

More particularly, this means that the following NN architecture (cf. Sec. 3.3) depends on the chosen parameters, though it can be adapted easily.

3.2. Preparing the Data

As described in Sec. 2, we get the detector images for Ne 1s and KLL Auger electrons from the simulation environment as presented by Hartmann et al. [8]. The kinetic energy of the 1s photoelectrons depends on the ionizing X-ray photon energy, which is set to 1180 eV in this case. This gives rise to Ne 1s electron energies centered at ~ 270 eV, while the Auger electron energies are independent of the X-ray photon energy, with the main peak lying at ~ 804 eV. However, these are perfectly simulated data, cf. Figs. 2a and 2b. In 2a, there is only one randomly placed Gaussian distribution present in the spectrogram.

The underlying pulse structure is neglected so far. To get closer to the real data, we add a pulse structure and noise to the simulated detector images. The last step of data preparation requires data normalization.

3.2.1. Adding a Pulse Structure to the Spectrogram

To achieve a SASE-like temporal structure in the spectrogram, we modulate the original Gaussian time distribution with a spiky intensity profile (cf. Fig. 1). We obtain the latter by generating a comb of Gaussian spikes with randomized amplitudes and spike durations as predicted by theory for a typical setting of an XFEL in ultrashort-pulse mode [27].

3.2.2. Adding Noise to the Detector Image

Additional noise is added to \mathcal{X} during training and testing as shown in Eq. 1. A given percentage p of the maximum intensity value x_{max} of $\mathbf{X} \in \mathcal{X}$ is used as an upper and lower bound of an equal distribution to draw w from:

$$\mathbf{X}_{\text{noisy}} = \left(x_{i,j} + (x_{\text{max}} \cdot w) \right)_{i=1, \dots, m, j=1, \dots, n}, w \sim \mathcal{G}(-p, p), \quad (1)$$

Figure 3 displays a detector image with different levels ($p \sim [0.0, 0.1, 0.2, 0.3]$) of added noise.

3.2.3. Normalizing the Data

It is evident, that the range of the intensity values differs from case to case. Especially when generating Auger data, cf. Fig. 2f, the intensities can get quite high compared to the Ne 1s data, cf. Fig. 2d. To counteract this, we perform a min-max-normalization for each $\mathbf{X} \in \mathcal{X}$. Therefore, the minimum (x_{min}) and maximum (x_{max}) intensity value of \mathbf{X} is used to perform the transformation for each pixel value x :

$$\mathbf{X}_{\text{norm}} = \left(\frac{x_{i,j} - x_{\text{min}}}{x_{\text{max}} - x_{\text{min}}} \right)_{i=1, \dots, m, j=1, \dots, n}, \quad (2)$$

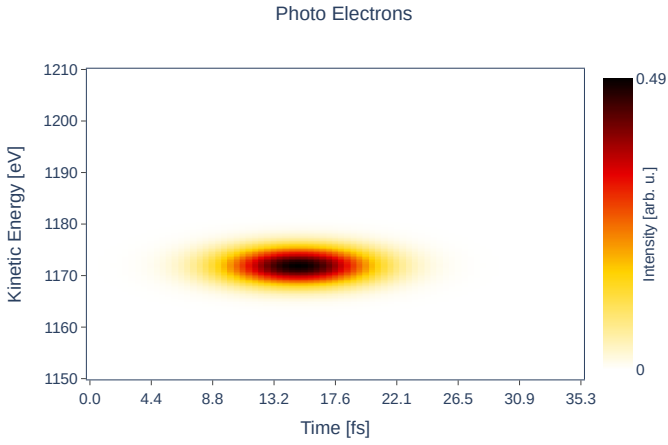
After normalization, all values in \mathbf{X}_{norm} are in the interval of $[0, 1]$.

3.3. Designing the Machine Learning Models

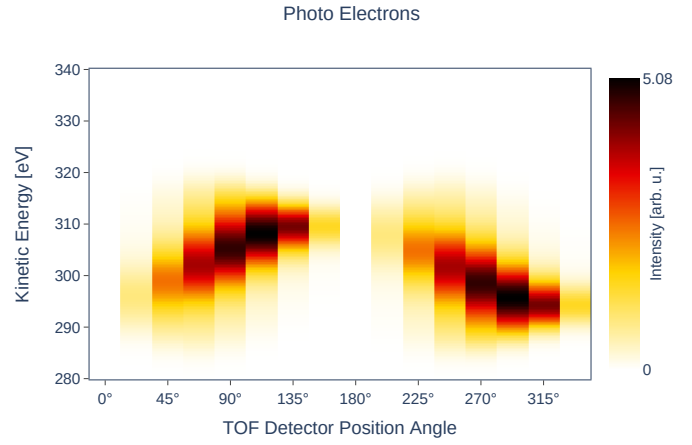
As we want to extract information from images, the most intuitive solution is to use a convolutional NN, which uses convolutions and pooling to extract low- and high-level features such as edges in the first component and a fully-connected NN for the actual label prediction.

3.3.1. Architecture

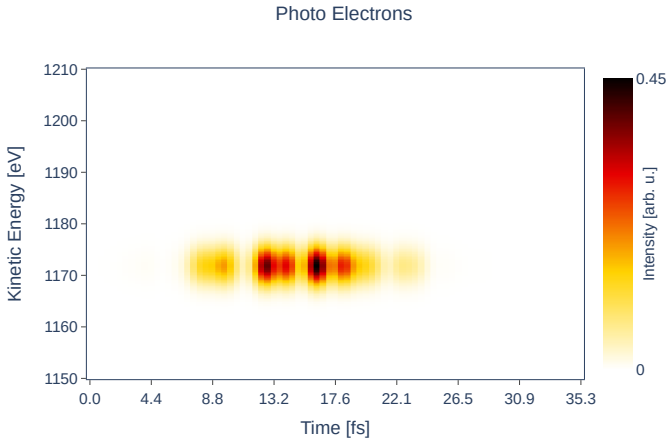
The most suitable network architecture for our problem is an NN with three convolutional blocks (cf. Fig. 4). Each block contains a convolutional layer, followed by an activation function and a max-pooling layer. The convolutional layers use a 3×3 kernel, stride of 1×1 and 1×1 zero-padding. The pooling layers use a 3×3 kernel, stride of 2×2 and 1×1 zero-padding. The network is specifically designed to cut both dimensions in half after each block. Thereby, a filter size of $[16, 32, 64]$ for the respective convolutional layers has proven to be sufficient. For the fully-connected component (except the last layer), we



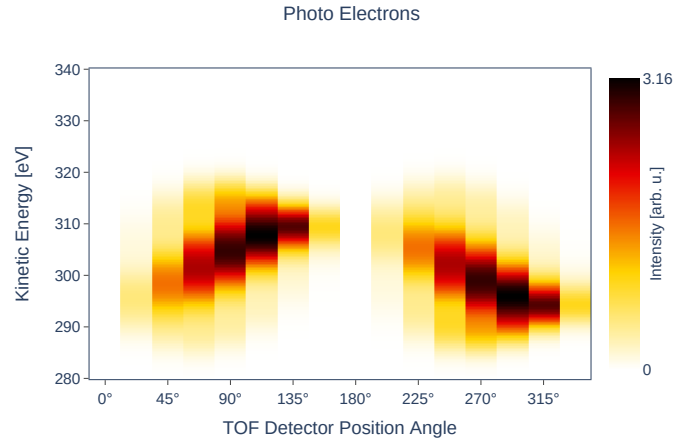
(a) Simulated spectrogram of SASE pulse as shown in [8].



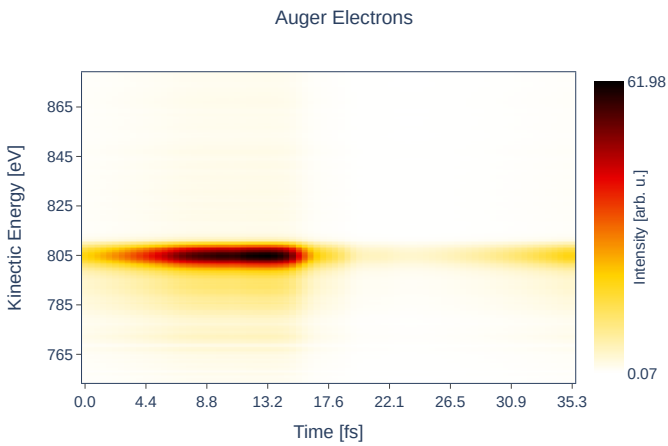
(b) Resulting simulated angularly streaked Ne 1s detector image from (a).



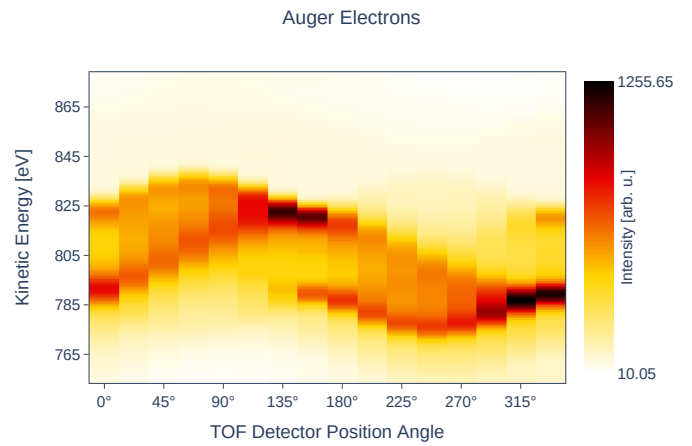
(c) Simulated spectrogram of SASE pulse after adding a pulse structure.



(d) Resulting simulated angularly streaked Ne 1s detector image from (c).



(e) Simulated spectrogram of Auger electrons with generic decay time of 6.5 fs.



(f) Resulting simulated angularly streaked Auger electron detector image from (e).

Figure 2: Created simulated Ne 1s data before [(a) and (b)] and after [(c) and (d)] adding a pulse structure. (e) and (f) display simulated angularly streaked Auger electron spectrogram and detector images, respectively, after adding a pulse structure.

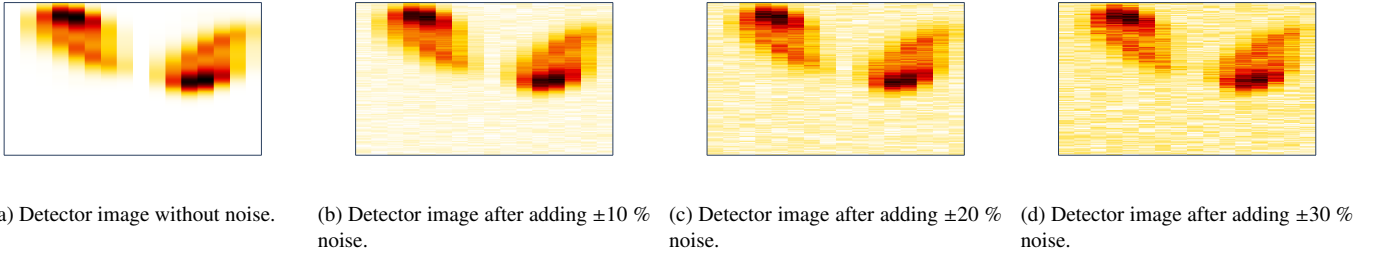


Figure 3: Adding different amount of noise levels to a simulated detector image.

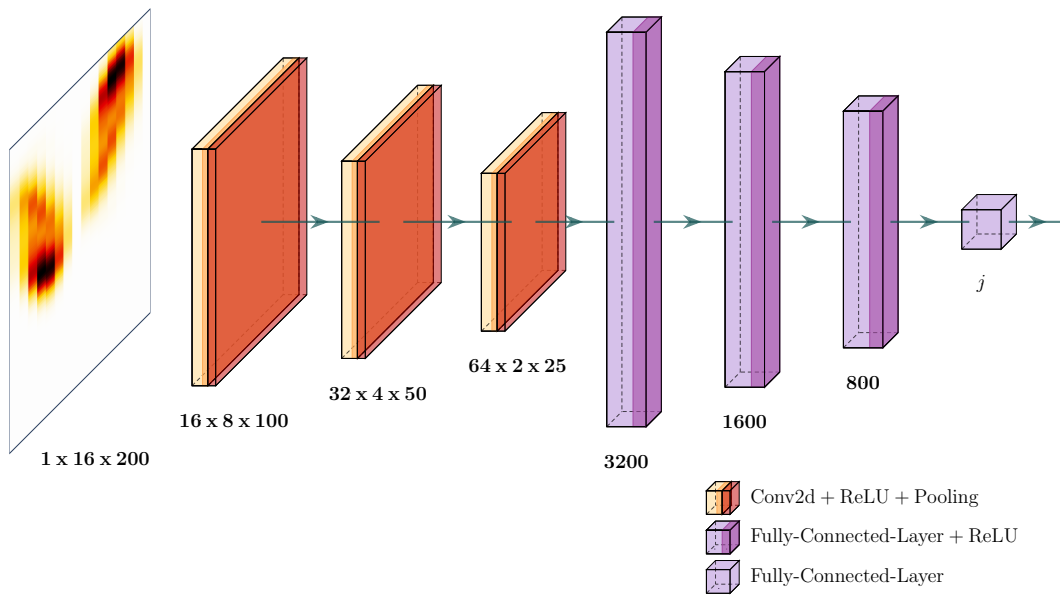


Figure 4: The here utilized convolutional neural network architecture.

use three layers with [3200, 1600, 800] neurons, respectively. The last layer of the fully-connected component depends on the label to predict, i.e., the size of j in \mathcal{L} . When predicting the *kick*, *pulse duration*, or *decay time*, $j = 1$. When predicting the *pulse structure*, j corresponds to the dimension of the spectrograms x-axis. We utilize the mean squared error loss function to train and optimize the network as the prediction of the pulse characteristics is a regression task in all cases.

3.3.2. Hyperparameter Optimization

The choice of architecture is not the only issue to be considered. Especially when training the NNs appropriately chosen hyperparameters are important to achieve efficient and goal-oriented training. Important parameters in this context are the *batch size*, *type of activation function*, *optimizer*, and *learning rate*. To find the best suitable combination of hyperparameters, we performed a grid-search with the following values:

- *Batch size*: [64, 128, 256, 512, 1024]

- *Activation function*: [ReLU, Sigmoid]
- *Optimizer*: [Adam, SGD (with Momentum)]
- *Learning rate*: [0.01, 0.001, 0.0001, 0.00001]

After NN training, we evaluated the respective parameter combinations according to the following criteria:

- *Criterion 1*: The test loss (after inputting $\mathcal{D}_{\text{test}}$ into the trained NN) should be minimal.
- *Criterion 2*: The parameter combination should be part of the best training runs. Therefore, we calculate the area under the test-run curve using the function's primitive. The runs with the smallest areas are considered to be the best, as it is assumed that the prediction error becomes small very fast. By applying this criterion, we ensure that the best test loss from *Criterion 1* is not a coincidence.

In general, it should be noted that there is not only one combination of hyperparameters that achieves good results during training. Nevertheless, there have been evident leaders. The best hyperparameter configurations regarding the individual labels are displayed in Tab. 1.

Label	BS	Act	Opt	LR
Kick	128	ReLU	Adam	0.0001
Pulse Duration	128	ReLU	SGD	0.0001
Decay	128	ReLU	SGD	0.001
Time Distribution	256	ReLU	Adam	0.001

Table 1: Best configuration of hyperparameters for the respective labels with BS = Batch size, Act = Activation function, Opt = Optimizer, and LR = Learning rate.

4. Results

All XFEL pulse characteristics can be predicted by utilizing NNs with varying degrees of accuracy. In particular, characteristics that cannot be extracted from the detector images directly are less accurately predicted. This applies mostly to the pulse duration and the time distribution of the SASE pulse. The kick and decay, however, are determined precisely in most cases. We will examine this in more detail in the following subsections.

4.1. Kick

Of all the characteristics studied, the kick turned out to be the easiest to predict. Fig. 5a shows that most of the predictions only slightly deviate from the targets. There are a couple of isolated outliers, but most of them do not exceed the limits of 1 and -1 eV. Nevertheless, an accurate estimate of this parameter is necessary for better judging the estimate of the characteristics *pulse duration* and *decay*. This will become apparent in the following sections.

4.2. Pulse Duration

The comparison of predicted and target pulse durations is shown in Fig. 5b. As for the kick estimations, the majority of pulse duration values are well estimated. However, it is evident that some of the values deviate strongly from the target values. One hypothesis explaining this behavior is that for smaller kicks predicting a pulse duration can become arbitrarily difficult (cf. Sec. 2). That is why we have investigated the accuracy of the pulse duration estimation against the true kick value.

Fig. 5c confirms the previously stated hypothesis. Above a kick value of approximately 5 eV, the estimation of the pulse duration becomes feasible. This is due to the fact that small kick values correlate to unsuccessful angular streaking shots that need to be discarded anyway. Fig. 6a and 6b display exemplary shots with a small and a large kick, respectively.

4.3. Decay

The decay value can also be well approximated by the respective NN (cf. Fig. 5d). Most of the estimates hardly deviate from the zero line of the difference for target minus prediction. However, as for the pulse duration values, there are some outliers strongly deviating from the true decay value. Using the same reasoning as for the pulse duration estimates, we have compared the prediction of the decay value with the true kick value. Here, the same behavior can be observed as for the pulse duration (cf. Fig. 5e). It is evident that a reasonable determination of the decay value is only possible for a kick value of 3 eV or higher. It follows that the decay cannot be predicted on a failed angular streaking shot either. Shots with small kick values should be discarded in advance to appropriately approximate the true decay value. Fig. 6c and 6d display exemplary shots with a small and a large kick for the decay reconstruction, respectively.

4.4. Pulse Structure

The full time-energy pulse structure of the SASE pulse is probably the most difficult property to predict. This is not surprising, as it is also the most complex one, being represented by a vector which holds the information of the intensity at 80 equally distributed time steps (mapped to a window of 35.3 fs later on, as this is the duration of one optical cycle for the chosen streaking wavelength $\lambda = 10.6 \mu\text{m}$ in [8]). We normalize the training data of the time distributions as for the previous labels and simplify the task for the NN. Altogether, the trained network works relatively well in its objective to predict the trend, i.e., peak positions and their relative intensities, of the pulse structure. However, as has been expected, the predictions are less accurate for more complex time distributions. This behavior can be seen for two different exemplary simulated SASE pulses in Fig. 8, one relatively simple (a) and one more complex (b), in which not all of the finer structures could be reliably reproduced. At the very least, the main features including the larger peaks can always be predicted.

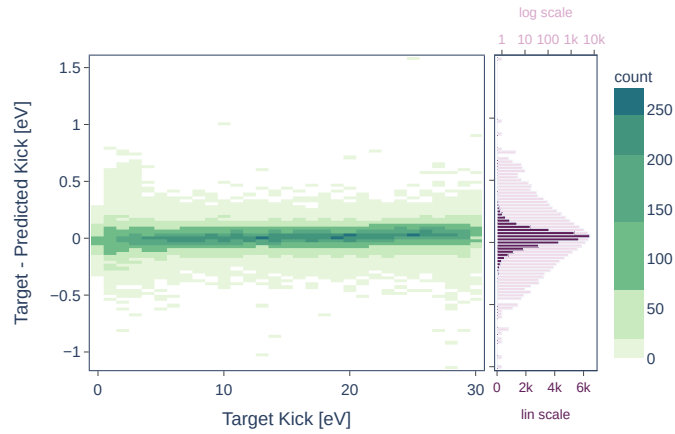
4.5. Influence of Noise on the NN Performance

In order to investigate the influence of noise on the predictions, we generated a test set comprising of several detector images with one ideal ($\pm 0\%$ noise) and one noisy ($\pm 30\%$ noise) expression per image and fed it into the NN.

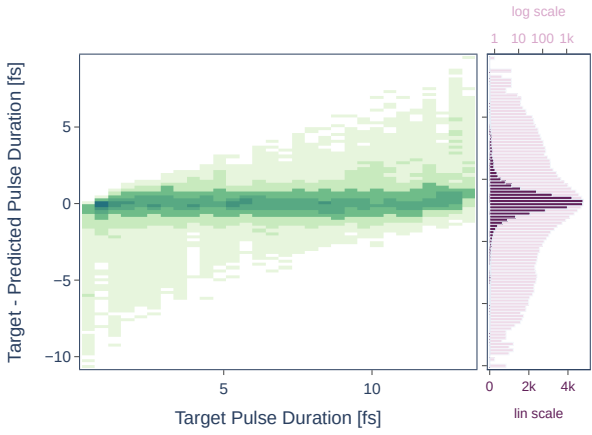
	Kick	Pulse Duration	Decay
$\pm 0\%$ Noise	0.07 eV	0.26 fs	0.07 fs
$\pm 30\%$ Noise	0.13 eV	0.54 fs	0.35 fs

Table 2: Prediction standard deviation computed on hundred samples per case. Settings for the kick and pulse duration sample data: *Kick* = 22.5 eV, *Pulse duration* = 4.85 fs. Additional settings for the decay data: *Decay* = 7.0 fs.

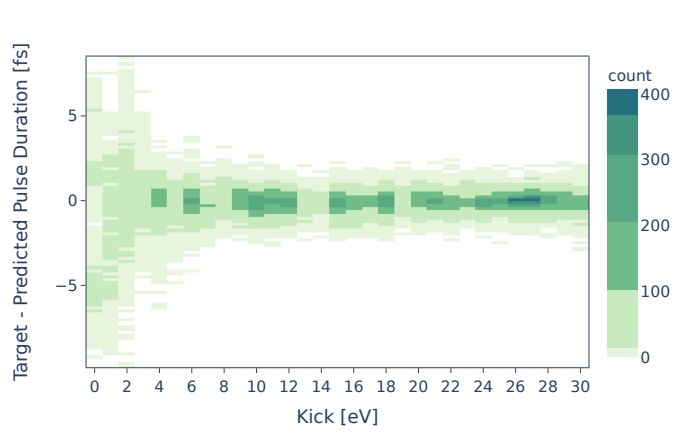
As expected, additional noise influences the result of the NN's prediction (cf. Tab. 2). Some expressive examples are shown in Fig. 5. The prediction for ideal data is almost perfect, whereas the prediction for noisy data slightly differs from the



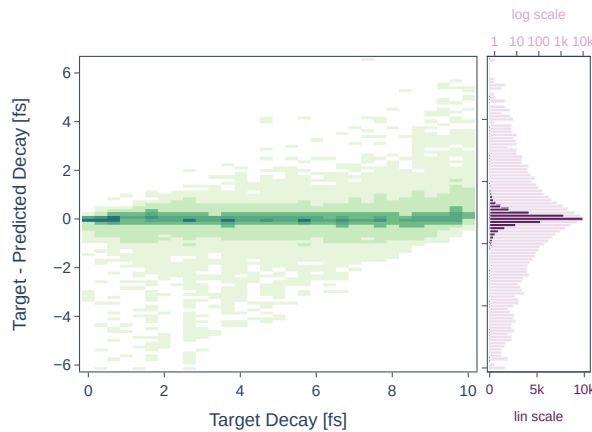
(a) Difference between the target and the predicted kick label, demonstrated on a test set with 40K samples. Most of the values predict the kick very accurately.



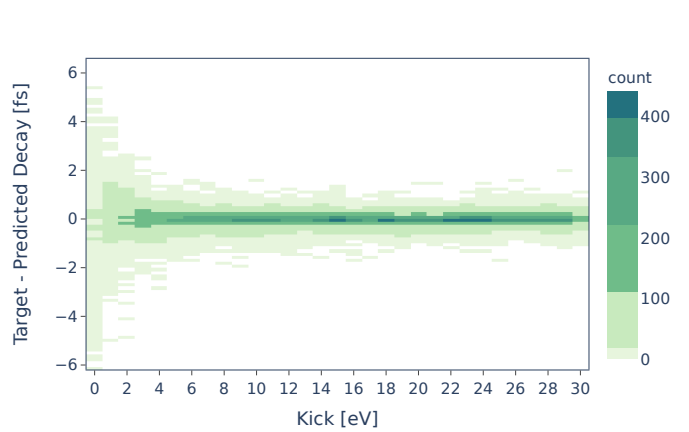
(b) Difference between the target and the predicted pulse duration label, demonstrated on a test set with 40K samples. There are several outliers that cannot be predicted by the utilized NN.



(c) Comparison of the pulse duration prediction regarding the size of the kick. The accuracy of the pulse length estimate depends on the respective kick value of the shot.



(d) Difference between the target and the predicted decay label, demonstrated on a test set with 40K samples. Although most predictions are sufficient, there are significant deviations from the target value.



(e) Comparison of the decay prediction regarding the size of the kick. The accuracy of the decay estimate depends on the respective kick value of the shot.

Figure 5: Prediction accuracies and dependencies of the labels *kick*, *pulse duration*, and *decay*.

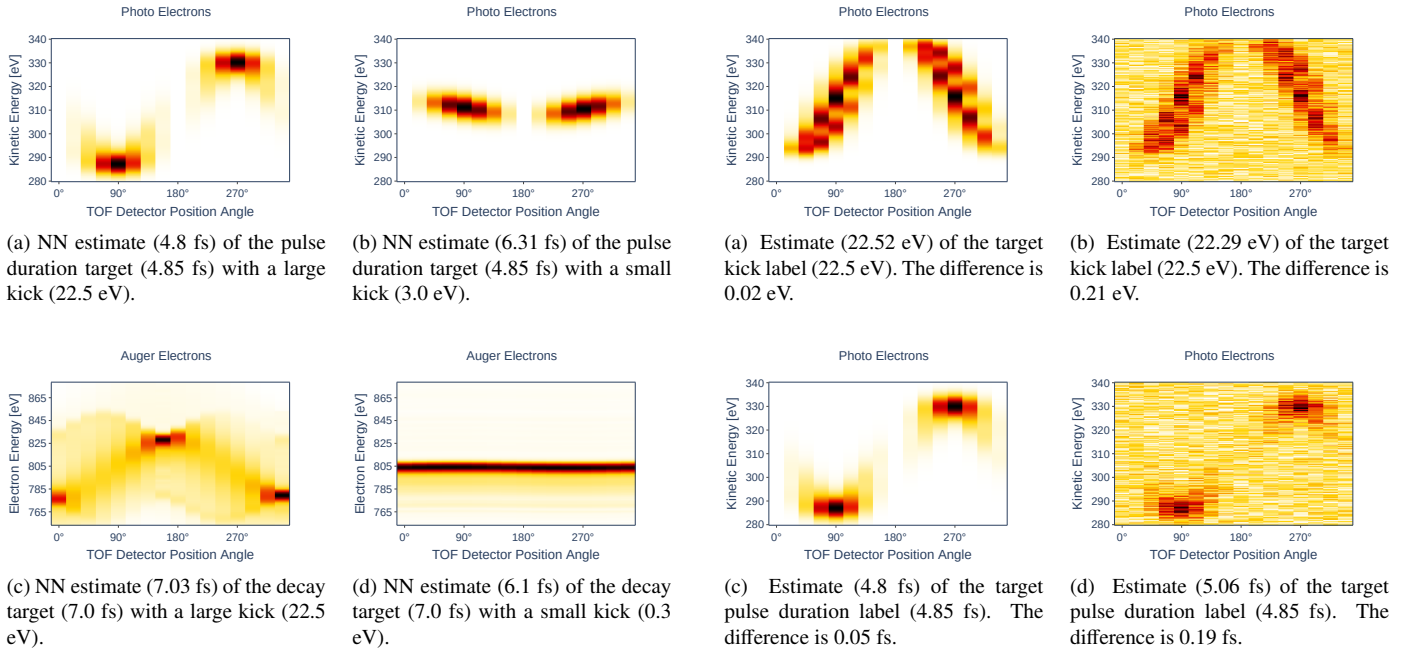


Figure 6: Exemplary selection of pulse duration and decay predictions with small and large kick value, respectively.

target. Despite the decreased prediction accuracies, it is evident that the NN can handle noise robustly.

5. Online SASE-Pulse Characterization

So far, we have shown that several characteristics of XFEL pulses are predictable with varying degrees of accuracy. To investigate how close the current status comes to real-time pulse characterization during experimental campaigns, we need to address different issues, which can each be tackled exploiting the specific analytical strength made accessible by the methods of NNs:

Output Speed. For an evaluation of the input images at the speed of the XFEL repetition rate under investigation, an efficient analysis is inevitable. NNs are known for delivering outputs quickly. We have used several batch sizes, starting from one image up to 4096 as input. Investigating this is important as such a comparison determines whether a batch-wise analysis is performing better than analyzing image-wise. Batch-wise evaluation is specifically suited for the European XFEL facility, since a train with a very fast succession of pulses is followed by a pause of several milliseconds that can be used for analysis purposes. We have tested how fast the NN output is generated on a GeForce RTX 2070 GPU (Tab. 3).

The model is able to reach quick predictions mostly independent of the batch size. In general, the number of input images in one batch is only limited by the RAM of the used GPU. Thus, it is apparent that it is advantageous to analyze a larger batch of data than individual images. With a batch size of 4096 our current model is already able to keep up with the European XFEL in high-repetition mode for online predictions.

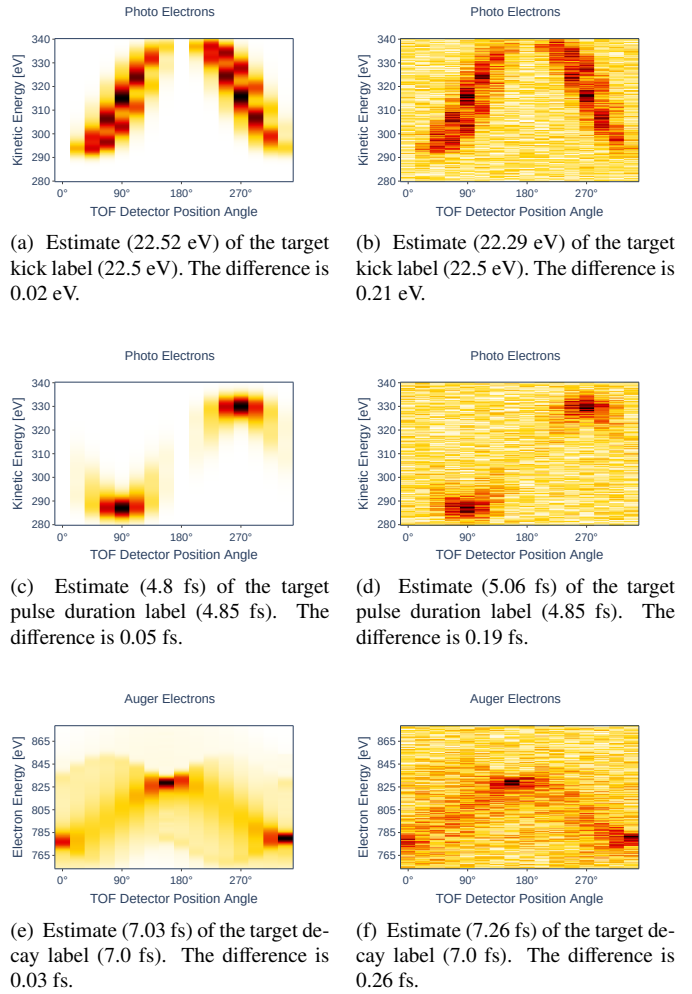


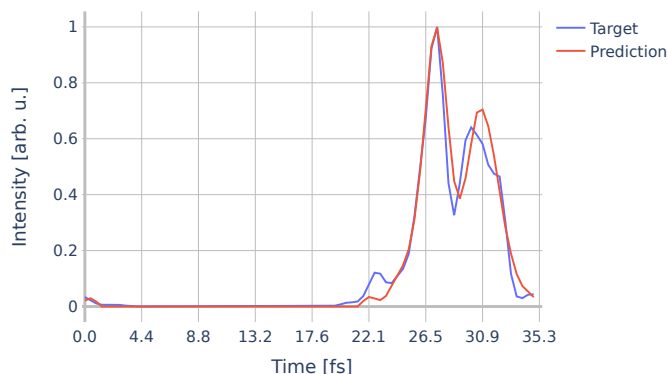
Figure 7: The influence of noise on the respective label estimate regarding one sample. (a), (c), (e) display estimates on data without additional noise. (b), (d), (f) show estimates of data with $\pm 30\%$ noise added.

BS	1	64	128	256	512	1024	2048	4096
Dur [ms]	1.38	1.44	1.48	1.54	1.62	1.54	1.38	1.44

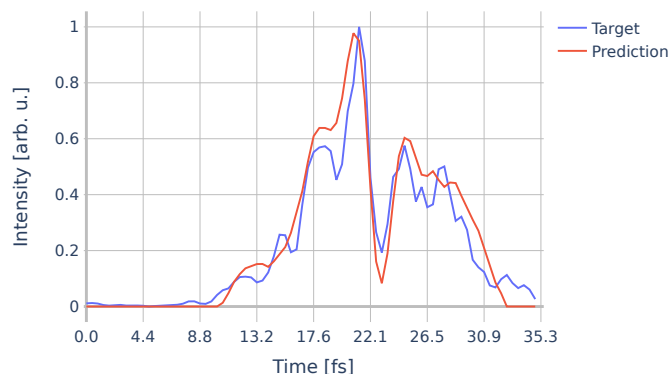
Table 3: Time measurements for predictions of the trained model on a GeForce RTX 2070 card with different batch sizes (BS).

Reliability Estimation. Next to fast evaluation, a degree of certainty in the NN predictions must be ensured. As shown in Sec. 4, the NN prediction may deviate quite substantially from the target. Some of the difficulties can be directly circumvented. By determining the kick, for example, we can already filter whether a prediction regarding the labels *decay* or *pulse duration* is reasonable. But this still does not give us a direct statement regarding how certain the NNs prediction is. Optimally, we would want to have a reliable measure of how good the predictions of the trained models are, even for unknown shots without a target.

There are several ways to determine the prediction uncertain-



(a) Simple SASE pulse time distribution.



(b) Complex SASE pulse time distribution.

Figure 8: Examples for a simple (a) and a more complex (b) simulated and reconstructed SASE pulse structure, respectively.

ties of NNs. The epistemic uncertainty determines the uncertainty of the model. This can be done, for example, via Monte Carlo dropout [32] or Monte Carlo batch normalization [33]. The aleatory uncertainty determines the uncertainty of the data. This can be done by creating a fitted cost function [34]. Both uncertainty determinations can be combined in one procedure as shown in [34].

Responding to Changes. So far, our NNs are suited only for data that look exactly like the input shown in Fig. 2. When utilizing real-life TOF spectrometers, it may occur that they fail or produce unrealistic results. In such cases NN re-training or knowledge extension is inevitable. Here, online learning [35] is a helpful tool. In this case, the model is trained sequentially with new data generated again and again. Thus, the training can be quickly adapted to new environments. To circumvent the catastrophic forgetting [36] of NNs, continual learning [37] may be utilized.

Gap between Simulation and Reality. In this article, we have shown that our developed NNs work on simulation data. Whether the NNs are suitable for predictions on experimental data is not easy to clarify, especially since we do not have true targets for the experiment data. In addition, we need to identify to what extent our modeled noise replicates the real noise of the spectrometer, e.g., electronic ringing of the detector readout. However, there are two ways to close the gap between simulation and experiment. Either the real data must be denoised before the analysis or the simulation data must be provided with additional, appropriately modeled noise. Simultaneous approaches in both directions should give a more complete understanding for mitigating this issue in future efforts.

6. Conclusion

In this article, we demonstrated a path toward online characterization of free-electron laser pulses by applying NN on de-

tor images captured with angular streaking. In addition to several predictable characteristics, we have been able to identify and confirm dependencies between the respective characteristics that can be used to control the machine settings during experimental campaigns. This way, the angular streaking technique has the potential to be leveraged from the proof-of-principle stage to a robust and highly advanced diagnostic for all free-electron laser facilities. In addition, the live updates on X-ray pulse changes may also be used for a more detailed control of the parameters and for actual SASE pulse shaping. Further steps to a successful implementation of these advanced methods involve closing the gap between simulation and experimental data through an instrument-specific treatment of the measurement noise and a reliable concept for error estimation, which we will investigate in future work.

CRedit Author Statement

Kristina Dingel: Conceptualization, Methodology, Software, Investigation, Writing - Original Draft, Visualization.

Thorsten Otto: Conceptualization, Methodology, Software, Investigation, Writing - Original Draft, Visualization.

Lutz Marder: Methodology, Software, Investigation, Writing - Original Draft, Visualization.

Lars Funke: Writing - Review & Editing, Visualization.

Arne Held: Writing - Review & Editing.

Sara Savio: Writing - Review & Editing.

Andreas Hans: Writing - Review & Editing.

Gregor Hartmann: Software, Writing - Review & Editing.

David Meier: Writing - Review & Editing.

Jens Viehhaus: Writing - Review & Editing.

Bernhard Sick: Writing - Review & Editing, Supervision, Funding acquisition.

Arno Ehresmann: Writing - Review & Editing.

Markus Ilchen: Conceptualization, Writing - Original Draft, Supervision.

Wolfram Helml: Conceptualization, Writing - Original Draft, Supervision, Project administration, Funding acquisition.

Acknowledgements

This research was supported by the project SpeAR-XFEL (05K19RKA) funded by the BMBF (German Federal Ministry of Education and Research). We gratefully acknowledge the assistance and support of the Joint Laboratory Artificial Intelligence Methods for Experiment Design (AIM-ED) between Helmholtzzentrum für Materialien und Energie, Berlin, and the University of Kassel.

Data and Code Availability

A repository containing the detector image analysis and according simulation data will be provided on request.

References

- [1] P. J. Ho, B. J. Daurer, M. F. Hantke, J. Bielecki, A. Al Haddad, M. Bucher, G. Doumy, K. R. Ferguson, L. Flückiger, T. Gorkhover, et al., The role of transient resonances for ultra-fast imaging of single sucrose nanoclusters, *Nature communications* 11 (1) (2020) 1–9.
- [2] L. Young, K. Ueda, M. Gühr, P. H. Bucksbaum, M. Simon, S. Mukamel, N. Rohringer, K. C. Prince, C. Masciovecchio, M. Meyer, et al., Roadmap of ultrafast x-ray atomic and molecular physics, *Journal of Physics B: Atomic, Molecular and Optical Physics* 51 (3) (2018) 032003.
- [3] U. Eichmann, H. Rottke, S. Meise, J.-E. Rubensson, J. Söderström, M. Agåker, C. Sätze, M. Meyer, T. Baumann, R. Boll, et al., Photon-recoil imaging: Expanding the view of nonlinear x-ray physics, *Science* 369 (6511) (2020) 1630–1633.
- [4] W. Decking, S. Abeghyan, P. Abramian, A. Abramsky, A. Aguirre, C. Albrecht, P. Alou, M. Altarelli, P. Altmann, K. Amyan, et al., A mhz-repetition-rate hard x-ray free-electron laser driven by a superconducting linear accelerator, *Nature Photonics* 14 (6) (2020) 391–397.
- [5] S. Milton, E. Gluskin, N. Arnold, C. Benson, W. Berg, S. Biedron, M. Borland, Y.-C. Chae, R. Dejus, P. Den Hartog, et al., Exponential gain and saturation of a self-amplified spontaneous emission free-electron laser, *Science* 292 (5524) (2001) 2037–2041.
- [6] S. Serkez, W. Decking, L. Froehlich, N. Gerasimova, J. Grünert, M. Guetg, M. Huttula, S. Karabekyan, A. Koch, V. Kocharyan, et al., Opportunities for two-color experiments in the soft x-ray regime at the european xfel, *Applied Sciences* 10 (8) (2020) 2728.
- [7] C. Behrens, F.-J. Decker, Y. Ding, V. Dolgashev, J. Frisch, Z. Huang, P. Krejčík, H. Loos, A. Lutman, T. Maxwell, et al., Few-femtosecond time-resolved measurements of x-ray free-electron lasers, *Nature communications* 5 (1) (2014) 1–7.
- [8] N. Hartmann, G. Hartmann, R. Heider, M. Wagner, M. Ilchen, J. Buck, A. Lindahl, C. Benko, J. Grünert, J. Krzywinski, et al., Attosecond time-energy structure of x-ray free-electron laser pulses, *Nature Photonics* 12 (4) (2018) 215.
- [9] J. Duris, S. Li, T. Driver, E. G. Champenois, J. P. MacArthur, A. A. Lutman, Z. Zhang, P. Rosenberger, J. W. Aldrich, R. Coffee, et al., Tunable isolated attosecond x-ray pulses with gigawatt peak power from a free-electron laser, *Nature Photonics* 14 (1) (2020) 30–36.
- [10] T. Driver, S. Li, E. G. Champenois, J. Duris, D. Ratner, T. J. Lane, P. Rosenberger, A. Al-Haddad, V. Averbukh, T. Barnard, et al., Attosecond transient absorption spectroscopy: a ghost imaging approach to ultrafast absorption spectroscopy, *Physical Chemistry Chemical Physics* 22 (5) (2020) 2704–2712.
- [11] R. Bonifacio, L. De Salvo, P. Pierini, N. Piovela, C. Pellegrini, Spectrum, temporal structure, and fluctuations in a high-gain free-electron laser starting from noise, *Phys. Rev. Lett.* 73 (1994) 70–73.
- [12] R. Neutze, R. Wouts, D. van der Spoel, E. Weckert, J. Hajdu, Potential for biomolecular imaging with femtosecond X-ray pulses., *Nature* 406 (6797) (2000) 752–7.
- [13] A. Barty, S. Boutet, M. J. Bogan, S. P. Hau-Riege, S. Marchesini, K. Sokolowski-Tinten, N. Stojanovic, R. Tobey, H. Ehrke, A. Cavalleri, S. Düsterer, M. Frank, S. Bajt, B. W. Woods, M. M. Seibert, J. Hajdu, R. Treusch, H. N. Chapman, Ultrafast single-shot diffraction imaging of nanoscale dynamics, *Nature Photonics* 2 (7) (2008) 415–419.
- [14] L. Young, E. P. Kanter, B. Krässig, Y. Li, A. M. March, S. T. Pratt, R. Santra, S. H. Southworth, N. Rohringer, L. F. Dimauro, G. Doumy, C. A. Roedig, N. Berrah, L. Fang, M. Hoener, P. H. Bucksbaum, J. P. Cryan, S. Ghimire, J. M. Glowina, D. A. Reis, J. D. Bozek, C. Bostedt, M. Messerschmidt, Femtosecond electronic response of atoms to ultra-intense X-rays., *Nature* 466 (7302) (2010) 56–61.
- [15] A. Rudenko, L. Inhester, K. Hanasaki, X. Li, S. J. Robatjazi, B. Erk, R. Boll, K. Toyota, Y. Hao, O. Vendrell, C. Bomme, E. Savelyev, B. Rudek, L. Foucar, S. H. Southworth, C. S. Lehmann, B. Kraessig, T. Marchenko, M. Simon, K. Ueda, K. R. Ferguson, M. Bucher, T. Gorkhover, S. Carron, R. Alonso-Mori, J. E. Koglin, J. Correa, G. J. Williams, S. Boutet, L. Young, C. Bostedt, S.-K. Son, R. Santra, D. Rolles, Femtosecond response of polyatomic molecules to ultra-intense hard X-rays, *Nature* 546 (7656) (2017) 129–132.
- [16] P. Eckle, M. Smolarski, P. Schlup, J. Biegert, A. Staudte, M. Schöffler, H. G. Müller, R. Dörner, U. Keller, Attosecond angular streaking, *Nature Physics* 4 (7) (2008) 565–570.
- [17] E. Constant, V. Taranukhin, A. Stolow, P. Corkum, Methods for the measurement of the duration of high-harmonic pulses, *Physical Review A* 56 (5) (1997) 3870–3878.
- [18] J. Itatani, F. Quéré, G. Yudin, M. Ivanov, F. Krausz, P. Corkum, Attosecond Streak Camera, *Physical Review Letters* 88 (17) (2002) 173903.
- [19] A. K. Kazansky, A. V. Bozhevolnov, I. P. Sazhina, N. M. Kabachnik, Interference effects in angular streaking with a rotating terahertz field, *Physical Review A* 93 (1) (2016) 013407.
- [20] M. R. Bionta, H. T. Lemke, J. P. Cryan, J. M. Glowina, C. Bostedt, M. Cammarata, J.-C. Castagna, Y. Ding, D. M. Fritz, A. R. Fry, J. Krzywinski, M. Messerschmidt, S. Schorb, M. L. Swiggers, R. N. Coffee, Spectral encoding of x-ray/optical relative delay., *Optics Express* 19 (22) (2011) 21855–65.
- [21] N. Hartmann, W. Helml, A. Galler, M. R. Bionta, J. Grünert, S. L. Molodtsov, K. R. Ferguson, S. Schorb, M. L. Swiggers, S. Carron, C. Bostedt, J.-C. Castagna, J. Bozek, J. M. Glowina, D. J. Kane, a. R. Fry, W. E. White, C. P. Hauri, T. Feuerer, R. N. Coffee, Sub-femtosecond precision measurement of relative X-ray arrival time for free-electron lasers, *Nature Photonics* 8 (July) (2014) 706–709.
- [22] M. Diez, A. Galler, S. Schulz, C. Boemer, R. N. Coffee, N. Hartmann, R. Heider, M. S. Wagner, W. Helml, T. Katayama, T. Sato, T. Sato, M. Yabashi, C. Bressler, A self-referenced in-situ arrival time monitor for X-ray free-electron lasers, *Scientific Reports* 11 (1) (2021) 3562.
- [23] T. Fuji, J. Rauschenberger, A. Apolonski, V. S. Yakovlev, G. Tempea, T. Udem, C. Gohle, T. W. Hänsch, W. Lehnert, M. Scherer, F. Krausz, Monolithic carrier-envelope phase-stabilization scheme, *Optics Letters* 30 (3) (2005) 332.
- [24] B. Rudek, S.-K. Son, L. Foucar, S. W. Epp, B. Erk, R. Hartmann, M. Adolph, R. Andritschke, A. Aquila, N. Berrah, et al., Ultra-efficient ionization of heavy atoms by intense x-ray free-electron laser pulses, *Nature photonics* 6 (12) (2012) 858–865.
- [25] A. Picón, C. S. Lehmann, C. Bostedt, A. Rudenko, A. Marinelli, T. Osipov, D. Rolles, N. Berrah, C. Bomme, M. Bucher, G. Doumy, B. Erk, K. R. Ferguson, T. Gorkhover, P. J. Ho, E. P. Kanter, B. Krässig, J. Krzywinski, A. A. Lutman, A. M. March, D. Moonshiram, D. Ray, L. Young, S. T. Pratt, S. H. Southworth, Hetero-site-specific X-ray pump-probe spectroscopy for femtosecond intramolecular dynamics, *Nature Communications* 7 (May) (2016) 11652.
- [26] X. Li, L. Inhester, T. Osipov, R. Boll, R. Coffee, J. Cryan, A. Gattton, T. Gorkhover, G. Hartman, M. Ilchen, et al., Electron-ion coincidence measurements of molecular dynamics with intense x-ray pulses, *Scientific reports* 11 (1) (2021) 1–12.
- [27] S. Krinsky, R. Gluckstern, Analysis of statistical correlations and intensity spiking in the self-amplified spontaneous-emission free-electron laser, *Physical Review Special Topics - Accelerators and Beams* 6 (5) (2003) 050701.

- [28] D. C. Haynes, M. Wurzer, A. Schletter, A. Al-Haddad, C. Blaga, C. Bostedt, J. Bozek, H. Bromberger, M. Bucher, A. Camper, S. Carron, R. Coffee, J. T. Costello, L. F. DiMauro, Y. Ding, K. Ferguson, I. Grguraš, W. Helml, M. C. Hoffmann, M. Ilchen, S. Jalas, N. M. Kabachnik, A. K. Kazansky, R. Kienberger, A. R. Maier, T. Maxwell, T. Mazza, M. Meyer, H. Park, J. Robinson, C. Roedig, H. Schlarb, R. Singla, F. Tellkamp, P. A. Walker, K. Zhang, G. Doumy, C. Behrens, A. L. Cavalieri, Clocking Auger electrons, *Nature Physics* 17 (4) (2021) 512–518. [arXiv:2003.10398](https://arxiv.org/abs/2003.10398).
- [29] R. Heider, M. S. Wagner, N. Hartmann, M. Ilchen, J. Buck, G. Hartmann, V. Shirvanyan, A. O. Lindahl, J. Grünert, J. Krzywinski, J. Liu, M. Ossiander, A. A. Lutman, T. Maxwell, A. A. Miahnahri, S. P. Moeller, M. Planas, J. Robinson, J. Viefhaus, T. Feuerer, R. Kienberger, R. N. Coffee, W. Helml, Megahertz-compatible angular streaking with few-femtosecond resolution at x-ray free-electron lasers, *Phys. Rev. A* 100 (2019) 053420.
- [30] S. Ren, K. He, R. Girshick, J. Sun, Faster R-CNN: Towards Real-Time Object Detection with Region Proposal Networks, Tech. rep. (2015).
- [31] C. Kyrkou, G. Plastiras, T. Theocharides, S. I. Venieris, C.-S. Bouganis, Dronet: Efficient convolutional neural network detector for real-time uav applications, in: 2018 Design, Automation Test in Europe Conference Exhibition, 2018, pp. 967–972.
- [32] Y. Gal, Z. A. Uk, Dropout as a Bayesian Approximation: Representing Model Uncertainty in Deep Learning Zoubin Ghahramani, Tech. rep. (jun 2016).
- [33] M. Teye, H. Azizpour, K. Smith, Bayesian Uncertainty Estimation for Batch Normalized Deep Networks, Tech. rep. (jul 2018).
- [34] A. Kendall, Y. Gal, What uncertainties do we need in bayesian deep learning for computer vision?, in: Proceedings of the 31st International Conference on Neural Information Processing Systems, 2017, pp. 5580–5590.
- [35] Ó. Fontenla-Romero, D. Martínez-Rego, B. Guijarro-Berdiñas, B. Pérez-Sánchez, D. Peteiro-Barral, Online machine learning, in: Efficiency and Scalability Methods for Computational Intellect, IGI Global, 2013, pp. 27–54.
- [36] J. Kirkpatrick, R. Pascanu, N. Rabinowitz, J. Veness, G. Desjardins, A. A. Rusu, K. Milan, J. Quan, T. Ramalho, A. Grabska-Barwinska, D. Hassabis, C. Clopath, D. Kumaran, R. Hadsell, Overcoming catastrophic forgetting in neural networks, *Proceedings of the National Academy of Sciences* 114 (13) (2017) 3521–3526.
- [37] G. I. Parisi, R. Kemker, J. L. Part, C. Kanan, S. Wermter, Continual lifelong learning with neural networks: A review, *Neural Networks* 113 (2019) 54–71.